Rock Mechanics Bulletin 5 (2026) 100262

Contents lists available at ScienceDirect

Rock Mechanics Bulletin

journal homepage: www.keaipublishing.com/en/journals/rock-mechanics-bulletin

Fast marching method-based bent-ray tracing for three-dimensional velocity imaging in mines

Jie Yang[a], Xueyi Shang[a,*], Linghao Liu[a], Yi Wang[b], Xibing Li[c]

[a] *State Key Laboratory of Coal Mine Disaster Dynamics and Control, School of Resources and Safety Engineering, Chongqing University, Chongqing, 400044, China*
[b] *State Key Laboratory of Geodesy and Earth's Dynamics, Innovation Academy for Precision Measurement Science and Technology, Chinese Academy of Sciences, Wuhan, 430077, China*
[c] *School of Resources and Safety Engineering, Central South University, Changsha, 410083, China*

ARTICLE INFO

Keywords:
Seismic tomography
Ray tracing
Mining-induced seismicity
Fast marching method
Three-dimensional velocity

ABSTRACT

Three-dimensional (3D) seismic velocity imaging is crucial for understanding rock mass stress and structures in mining. Conventional straight-ray tomography suffers from ray-path mismatches with true wavefield propagation in complex media, leading to reduced velocity model accuracy. To address this, we propose a 3D velocity imaging method that integrates the Fast Marching Method (FMM) for bent-ray tracing with the Algebraic Reconstruction Technique (ART) for velocity inversion. The proposed approach was validated through checkerboard tests, recovery tests, and laboratory Lead-Break experiments. Results show that FMM-based ray tracing significantly improves inversion accuracy, achieving root-mean-square (RMS) travel-time residuals of 1.39 ms and 28.66 ms in recovery and field tests, corresponding to reductions of 76.6% and 18.6% compared with straight ray tracing-based methods. Application in the Yongshaba mine, Guizhou Province, China, revealed a distinct low-velocity zone surrounded by high-velocity regions, which is consistent with mining activities and excavation plans. This study demonstrates that the FMM-ART framework provides a robust and accurate tool for mine-scale velocity imaging, with implications for monitoring stress evolution, improving safety, and potential integration with real-time monitoring.

1. Introduction

Rock mass properties are highly related to seismic wave velocity, and velocity imaging analysis has been widely used in fields such as mine engineering, petroleum engineering, and underground engineering (Bhagade et al., 2021; Niu et al., 2025). Since the 1970s, velocity imaging has been employed to explore Earth's internal structure, with early studies such as Dziewonski et al. (1977) and Aki (1977), who successfully obtained the crustal structure beneath California. With advances in computing capacity and the availability of high-quality seismic data, seismic velocity imaging gradually evolved into a distinct research field (Zhao, 2001). Over the past decades, it has been widely applied to various geoscientific problems, including the detection of lower mantle plumes (Hwang et al., 2011), the investigation of the Cascadia subduction zone (Chen et al., 2015), and the analysis of fault dip angles and crustal heterogeneity near fault zones (O'Connell et al., 2007). More recently, tomography techniques have been extended to engineering and applied geophysics, such as examining the correlation between seismic velocity and rock mass stress (Brantut, 2018; Dong et al., 2024), conducting P-wave velocity imaging of surrounding rock ahead of tunnel faces to extend the exploration range of boreholes (Liu et al., 2024), and characterizing rock mass velocity structures in underground engineering (Wang et al., 2023).

Three-dimensional seismic velocity imaging is particularly important in mining, as it enables detailed characterization of rock mass structures and stress distributions, which are essential for safe excavation and stability assessment. Generally, high stress tends to close pre-existing fractures, resulting in high-velocity zones, while excavation and blasting damage will lead to low-velocity zones (Seya et al., 1979; Young and Maxwell, 1992). Mining areas are typical regions with human activity, where significant changes in internal structures can occur in a short period, such as surface subsidence and fault slippage (Ziegler et al., 2015; Zhou et al., 2022; Wang et al., 2025). These changes are usually accompanied by many microseismic events, which provide a

---

* Corresponding author.
E-mail address: shangxueyi@cqu.edu.cn (X. Shang).

Peer review under the responsibility of Chinese Society for Rock Mechanics & Engineering.

https://doi.org/10.1016/j.rockmb.2025.100262
Received 11 June 2025; Received in revised form 17 September 2025; Accepted 16 October 2025
Available online 25 October 2025

wealth of data resources for seismic tomography (Łukasz et al., 2021). Traveltime tomography is widely used for velocity structure imaging due to its mature theory, efficiency, and accuracy (Huang and Zhao, 2006). In travel-time tomography, ray tracing travel-time calculation is crucial, as it directly determines the accuracy and efficiency of the tomographic inversion.

However, the ray-tracing methods currently used in mining tomography still have significant limitations. Straight-ray, shooting, or pseudo-bending methods are commonly used in mining tomography (Julian and Gubbins, 1977; Vidale, 1989; Wang et al., 2018; Song et al., 2024). Among them, the traditional straight-ray method often produces ray-path mismatches with the true wavefield in complex mining environments, resulting in low imaging accuracy and non-unique solutions. Pseudo-bending and shooting provide certain improvements, but they are prone to local minima in complex media and suffer from low computational efficiency in large-scale 3D models. Furthermore, the finite-difference method can be used to solve the Eikonal equation and calculate travel times and ray paths in a 3D velocity model. The Fast Marching Method (FMM) is a widely used approach (Dong et al., 2021), offering significant advantages in computational accuracy, efficiency, and stability, while being consistent with seismic wave propagation laws. It has been successfully applied in regional tomography, for example, in Rawlinson and Sambridge (2004) for studying underground structures in Australia.

To address the challenges of local minima, low computational efficiency, and reduced accuracy encountered in complex media (e.g., mines) when using straight-ray, shooting, or bending techniques, this study proposes a 3D velocity imaging method for mines by combining the FMM and Algebraic Reconstruction Technique (ART). The main innovations and contributions are: (1) The proposed method enables the FMM-based first-arrival wave travel-time calculation, demonstrating its adaptability to complex media like mines and offering good computational efficiency. (2) The ART incorporating a relaxation factor serves as the reconstruction algorithm for the 3D velocity model, achieving high accuracy in the reconstruction results. (3) The proposed method shows promising performance in synthetic tests, with a root-mean-square (RMS) of the residual travel time of only 1.39 ms, and the imaging results from engineering applications align well with the mining activities.

The remaining sections are organized as follows. Section 2 presents the 3D velocity imaging method for mines based on the FMM and ART. Section 3 conducts synthetic tests and performs comparative analysis. Section 4 applies the method to process actual mining data, obtain tomographic inversion images, and provide interpretations. Section 5 provides a detailed discussion of the FMM and ART and explores prospects in depth. Section 6 provides a comprehensive conclusion to the study.

2. Methodology

This study develops a three-dimensional seismic velocity imaging framework by integrating the FMM for ray-path calculation with the ART for model inversion. The process begins with the input of microseismic data (arrival travel times, source locations, and sensor locations), followed by ray tracing using FMM to calculate P-wave travel times and propagation paths. These results are then incorporated into ART, which iteratively reconstructs the velocity model with the aid of a relaxation factor to improve convergence and accuracy. The synthetic tests (checkerboard tests and recovery tests) in this study were performed using the same source–sensor geometry as the Yongshaba dataset to evaluate the method's ability to recover the velocity model. The same workflow was then applied to the field data, and the imaging results were evaluated in conjunction with the mining plan.

2.1. Ray tracing technique based on the FMM

Traditional finite-difference schemes for solving the eikonal equation were first introduced by Vidale (1988), who determined wavefront expansion by continuously computing first-arrival travel times at discrete grid points. However, this approach only allowed outward propagation of the wavefront, which deviates from physical laws and performs poorly in complex models. To address these limitations, Sethian (1996) proposed the Fast Marching Method (FMM), which has become a widely adopted technique for seismic ray tracing. Unlike straight-ray or pseudo-bending methods that often suffer from mismatches with true wave propagation, FMM solves the eikonal equation using an upwind finite-difference scheme and updates travel times across the grid in a stable and efficient manner. By ensuring that ray paths strictly follow wavefront propagation principles, FMM provides unconditional stability, good flexibility, and significantly improved accuracy in heterogeneous media, thereby enhancing the reliability of velocity imaging in mining environments.

The FMM uses a finite-difference upwind scheme to solve the time gradient of the eikonal equation. The upwind difference method is flexible and unconditionally stable. Sethian provided a constructive demonstration of the unconditional stability of this scheme. It effectively addresses issues such as topological changes, corners, and cusps that occur during the propagation of seismic wavefronts in complex media. In two dimensions (the x and z directions), the eikonal equation governing seismic wave propagation is expressed as follows,

$$\frac{\partial t(x,z)^2}{\partial x^2} + \frac{\partial t(x,z)^2}{\partial z^2} = s^2(x,z) \tag{1}$$

where t represents the travel time of the first-arrival seismic wave, s denotes the slowness of the medium, and x and z are the coordinates.

To calculate the travel time of seismic waves, Eq. (1) is discretized using the upwind difference scheme, resulting in the following expression,

$$\left[\max\left(D_{i,j}^{-x}t, -D_{i,j}^{+x}t, 0\right)^2 + \max\left(D_{i,j}^{-z}t, -D_{i,j}^{+z}t, 0\right)^2\right]^{\frac{1}{2}} = s_{i,j} \tag{2}$$

where $D_{i,j}^{-x}t$, $D_{i,j}^{+x}t$, $D_{i,j}^{-z}t$, and $D_{i,j}^{+z}t$ represent the forward and backward difference operators for the travel time t at the point (i, j) in the x and z directions, the schematic diagram of the difference scheme is shown in Fig. 1.

Then, the first-order upwind difference operators along the x and z directions are given by,

$$\begin{aligned} D_{i,j}^{-x}t &= \frac{t_{i,j} - t_{i,j-1}}{\Delta x}, D_{i,j}^{+x}t = \frac{t_{i,j+1} - t_{i,j}}{\Delta x} \\ D_{i,j}^{-z}t &= \frac{t_{i,j} - t_{i-1,j}}{\Delta z}, D_{i,j}^{+z}t = \frac{t_{i+1,j} - t_{i,j}}{\Delta z} \end{aligned} \tag{3}$$

Moreover, the second-order upwind difference operators along the x and z directions are given by,

$$\begin{aligned} D_{i,j}^{-x}t &= \frac{3t_{i,j} - 4t_{i,j-1} + t_{i,j-2}}{2\Delta x}, D_{i,j}^{+x}t = \frac{3t_{i,j} - 4t_{i,j+1} + t_{i,j+2}}{2\Delta x} \\ D_{i,j}^{-z}t &= \frac{3t_{i,j} - 4t_{i-1,j} + t_{i-2,j}}{2\Delta z}, D_{i,j}^{+z}t = \frac{3t_{i,j} - 4t_{i+1,j} + t_{i+2,j}}{2\Delta z} \end{aligned} \tag{4}$$

The process involves solving the discrete eikonal equation to obtain the travel time t: First, the target point and its surrounding points with known travel times are selected according to the wavefront expansion principle, and an appropriate difference scheme is then applied to the target point. When the wavefront is expanding outward, the travel time of the unknown point is computed using backward differences based on the points on the current wavefront. Conversely, forward differences are applied to calculate the travel time when the wavefront propagates inward. In general, based on the direction of wavefront expansion, a quadratic equation is established at the unknown point using forward and backward difference schemes in that direction. The larger root of this equation is then selected as the travel time of that point.

In the implementation of the FMM, a narrowband technique is used to simulate the expansion of the wavefront (Fig. 2). This involves using a

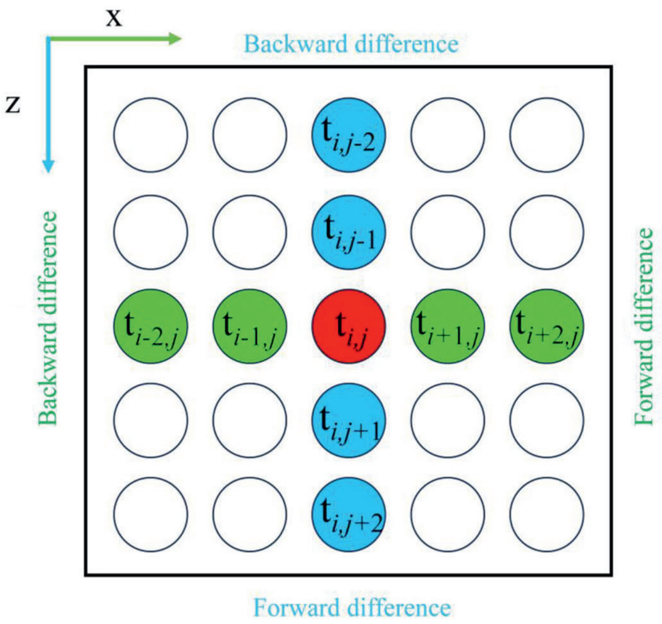

Fig. 1. Schematic diagram of the difference scheme in two dimensions along the two directions.

narrowband around the wavefront to separate known points from unknown points, identifying the point with the minimum travel time within the narrowband as the new wavefront expansion point. This approach simulates wavefront expansion in accordance with the principle of "entropy conservation" during seismic wave propagation. The narrowband technique classifies all computed grid points into three categories: Accepted points (points whose travel time calculation has been completed); Narrowband points (points that are approximately on the wavefront); and Far away points (points whose travel time has not yet been calculated). Initially, the source point is the only point with a completed travel-time calculation; several neighboring points around the source are classified as Narrowband points, and all remaining points are treated as Far-away points. The basic steps of the narrowband technique are given as follows:

(1) First, set the source point as the Accepted point with a travel time of zero, while other points are set as Far away points with travel times of infinity.
(2) Then, calculate the travel times of four points (up, down, left, right) around the source, and place these values within the narrowband to establish the initial narrowband.
(3) Search for the point with the minimum travel time within the narrowband and add it to the Accepted points. After that, the upwind difference is used to calculate the travel times of the Far away points, which are included in the narrowband.
(4) Repeat step (3) and update the travel times of the points that meet the minimum travel time condition and select the minimum travel time. Continue this process until the narrowband is empty and stop the calculations.

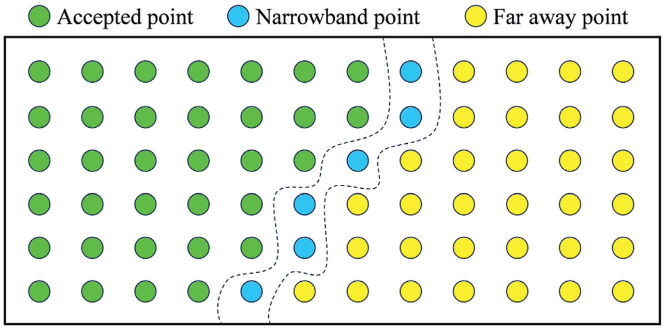

Fig. 2. Schematic diagram of the narrowband technique. The dashed lines indicate the narrowband area. The legends of the colored circles are shown at the top.

The open-source Python package pyekfmm written by Chen et al. (2023) was used to implement the FMM. The functions fmm and stream from the package are used to compute travel times and ray paths, where the fmm function is employed to solve the eikonal equation, resulting in the travel time field across the entire modeling range; the stream function calculates the ray paths based on the travel time field. Fig. 3 presents several examples of ray tracing using the FMM, showing the ray paths from some of the microseismic events used in this study to the sensors.

2.2. ART image reconstruction algorithm

ART is an iterative image reconstruction technique. Its primary idea is to solve linear equations for image reconstruction. In the ART application for mine seismic tomography inversion, the image is discretized into an $n \times n$ rectangular grid, where the slowness of each grid is denoted as f_j and the total number of grids is marked as N. The reconstruction process can be expressed as linear equations,

$$p_i = \sum\nolimits_{j=1}^{N} w_{ij} f_j \tag{5}$$

where p_i represents the travel time of a specific ray, and w_{ij} denotes the length of that ray in a particular grid cell.

The ART employs an iterative approach to approximate the true solution. The model is updated along individual ray paths, with each travel-time residual distributed over its corresponding path. The slowness of each grid cell is adjusted proportionally according to the lengths of the ray path segments within the cell. Each equation can be treated as a hyperplane in an N-dimensional space during the iterative process. The final image is obtained by continuously iterating and approaching the intersection point of these hyperplanes.

In practical mining applications, interfering factors such as noise may cause the iterations to converge to multiple possible solutions. A relaxation factor λ is introduced into the algorithm to address this issue. This factor adjust the difference between the initial and corrected slowness during the iteration process, bringing the estimates closer to the actual slowness, thereby reducing the reconstruction error. The relationship between the estimate value and relaxation factor can be expressed as,

$$f_{k+1}^{j} = f_{k}^{j} + \lambda_k \frac{\left(p_i - \sum_{j=1}^{N} w_{ij} f_{k}^{j}\right)}{\sum_{j=1}^{N} w_{ij}^{2}} w_{ij} \tag{6}$$

where f_{k+1}^{j} represents the estimated value of the j slowness at the $k+1$ iteration, f_{k}^{j} denotes the estimated value of the j slowness at the k iteration, and λ_k indicates the relaxation factor at the k iteration.

2.3. Velocity imaging method based on the FMM and ART

In this study, FMM is employed to trace seismic wave propagation paths and obtain travel-time and path information, which are then used in ART for velocity image reconstruction. The imaging workflow is illustrated in Fig. 4, and the specific steps are as follows,

(1) Input of microseismic dataset: The first-arrival times of P-waves, together with the source and sensor locations of microseismic events, are imported into the model to provide the fundamental observational constraints.

(2) Establishment of the 3D grid and initial velocity model: The study area (3900 m × 1800 m × 300 m) is discretized into a three-dimensional grid with a spacing of 50 m. An initial velocity model is then determined based on actual site conditions, balancing computational efficiency with the required imaging accuracy.
(3) Ray tracing and travel-time calculation: the FMM is applied to compute seismic ray paths and their corresponding theoretical travel times between sources and sensors, ensuring accurate path estimation in complex media.
(4) Relaxation factor selection and velocity inversion: The optimal relaxation factor is determined from the relaxation factor curve, balancing convergence stability and accuracy. Subsequently, the ART is employed to iteratively update the velocity model based on the travel-time residuals. Outliers are handled during the inversion process to obtain the final three-dimensional velocity model.

3. Synthetic tests

3.1. Checkerboard test

The checkerboard test is a commonly used technique in seismology to evaluate imaging quality. In this test, a series of known subsurface models are constructed (e.g., alternating high- and low-velocity blocks in a checkerboard pattern). These models are then subjected to tomographic inversion, and the recovered images are compared with the input models to assess imaging accuracy.

For the synthetic test, the source and sensor locations were derived from actual data from the Yongshaba mine (Fig. 5), and they were expressed in relative coordinates. The distributions of seismic events and sensors were identical to those in the engineering application described in Section 4. The sensor arrangement spanned the 930 m, 1070 m, and 1120 m levels. The recorded microseismic events were widely distributed throughout the study volume, providing good ray coverage.

The synthetic velocity model assumes a background velocity of 5000 m/s, with a ±5% perturbation applied to each grid cell so that adjacent cells have opposite signs. The grid spacing is 50 m, and the modeling domain matches the subsequent field application (Section 4). The resulting synthetic model serves as the input velocity model. The travel-time dataset is computed using the same rays as the actual data, which is then augmented with random errors comparable to the picking accuracy. These random errors are drawn from a zero-mean Gaussian distribution with a standard deviation of 0.001 s. The noisy dataset is treated as the observed data for velocity imaging. Then, a tomographic inversion is performed based on the proposed velocity imaging method, ultimately yielding the output model for the checkerboard test. The output model is compared with the corresponding input model to evaluate the inversion accuracy and robustness of the method (Fig. 6). The checkerboard test provides a stringent resolution assessment;

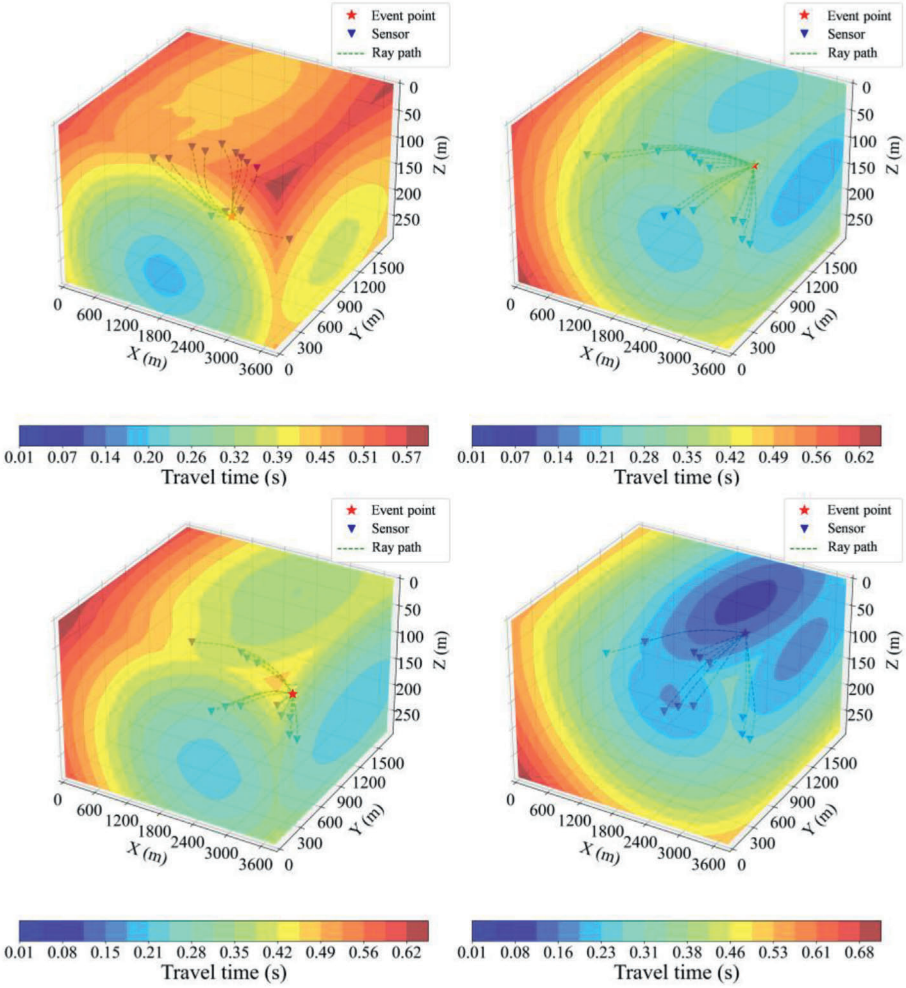

Fig. 3. Schematic diagram of the FMM ray tracing. The red pentagram and blue triangle represent the source and sensor, respectively. The green dashed curve illustrates the ray path. The distribution of travel times at each spatial location is shown at the bottom.

locations where the input and output V_p perturbations share the same sign are considered well reconstructed. The results indicate that the main area within the 970–1150 m depth range is well recovered. By contrast, recovery near the 910 m layer is limited to a small portion of the region.

3.2. Recovery test

Recovery tests can be used to assess the advantages and limitations of seismic data processing methods, validate the accuracy and robustness of algorithms, and optimize parameter selection and workflows, thereby improving the quality and reliability of data processing. Therefore, recovery tests were conducted to further verify the reliability of the distribution characteristics of high- and low-velocity zones obtained from the inversion. The input model follows the configuration described in Wang et al. (2018). The ray paths and travel times are determined by the FMM ray tracing. Subsequently, Gaussian noise with a standard deviation of 0.001 s is added to the travel times, and the resulting noisy data are used as synthetic travel-time inputs for inversion. As shown in Fig. 7, the recovery test results indicate that the major low-velocity zones and the surrounding high-velocity zones are well recovered. Moreover, several continuous low-velocity zones along the mining tunnel are visible in the output model. The shape and extent of these zones are generally similar to those of the input model, suggesting that they can be treated as reliable features. Horizontally, the high-velocity zones surrounding the low-velocity zones along the mining tunnel are generally recoverable in the output model.

It can be seen that there are some unsatisfactory restoration areas, such as the low-velocity zone at the 970 m level and the high-velocity zone at the 1030 m level. Fig. 8 illustrates the specific ray distribution. The results clearly demonstrate that image quality is strongly controlled by ray coverage density and distribution characteristics. There are 9304, 17,027, 14,254, 12,658, and 6646 rays for the 1150 m, 1090 m, 1030 m, 970 m, and 910 m levels, respectively. At the depth of

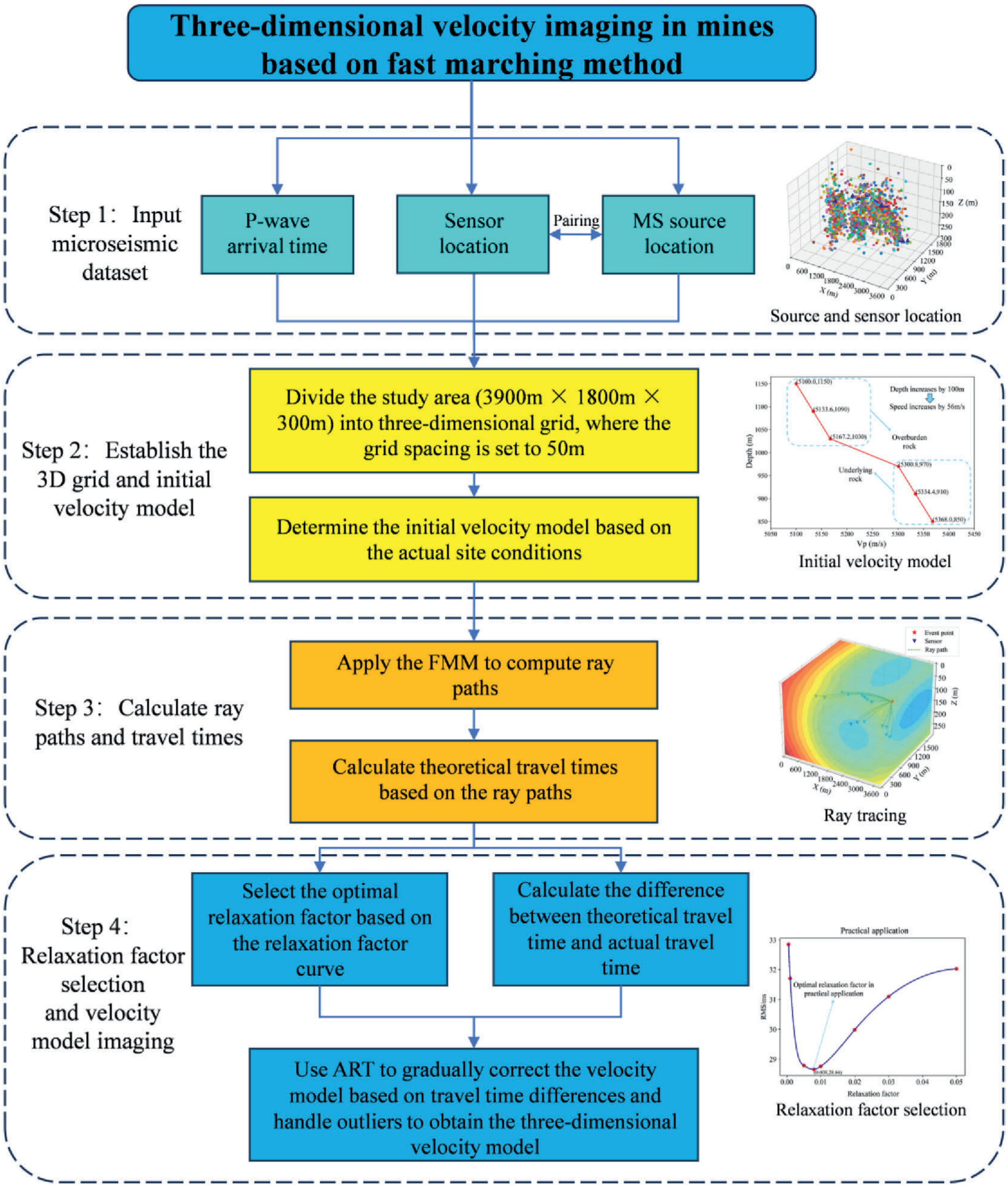

Fig. 4. Flowchart of the proposed velocity imaging method.

$Z = 1090$ m, where the number of rays is the largest and their distribution is relatively uniform with good multi-azimuthal crossing, the FMM method successfully recovers the shape and boundaries of the velocity anomalies. In contrast, at $Z = 1030$ m and $Z = 970$ m, the regions marked by black boxes in Fig. 8 exhibit sparse and directionally concentrated ray coverage, leading to significant distortions in the inversion results. In these areas, the FMM method produces blurred or even broken anomaly boundaries, while the straight-ray method suffers from stronger streaking and artifacts, with anomalies being elongated, misplaced, or even locally absent. The underlying reason is that insufficient ray coverage provides weak constraints for the inversion equations, especially when near-source and near-receiver paths are short, limiting penetration through low-velocity anomalies and thus reducing sensitivity to travel-time perturbations. Moreover, heterogeneity in velocity causes ray bending, creating shadow zones or regions of concentrated ray density, which further aggravates the uneven imaging resolution. Overall, Figs. 7 and 8 jointly demonstrate that ray distribution directly determines imaging quality: both high density and multi-azimuthal crossing are critical for accurate recovery of anomalies. In regions with good ray coverage, the FMM method clearly outperforms the straight-ray method because it accounts for ray bending effects.

The velocity model perturbation map obtained from the recovery test is shown in Fig. 9. The velocity perturbations are relative to the initial velocity model used during the inversion. Compared with the straight line-based result, the perturbations obtained using FMM are more consistent with those of the input model, demonstrating higher reliability in the recovery of both low-velocity and high-velocity zones. In addition, the RMS of the travel-time residuals is calculated to assess the inversion results quantitatively. First, forward modeling of the inverted velocity model is performed to obtain the theoretical travel times between each microseismic event and the triggered sensors. Next, the travel-time residuals are calculated by subtracting the theoretical travel times of the inverted model from those obtained through forward modeling of the input model. The travel-time residuals are all squared, summed, and divided by the total number of residuals to obtain the mean of the squared residuals. Finally, the square root of this mean is used to obtain the RMS of the travel-time residuals. Generally, a smaller RMS of the travel-time residuals indicates a better inversion result. The RMS of travel-time residuals obtained using the fast marching method is 1.39 ms, which is superior to the 5.94 ms obtained using the straight line method.

3.3. Lead-break experiment validation

To verify the applicability of the FMM-based travel-time three-dimensional velocity imaging method, an indoor acoustic emission lead-break experiment was conducted on a granite specimen with a single circular hole. The granite sample used in the experiment measures 30 cm × 20 cm × 10 cm and exhibits a P-wave velocity of 6110 m/s. A cylindrical hole with a diameter of 50 mm was drilled at the center (15, 10) cm of the sample, thus producing a specimen with a single circular cavity. One of the 30 cm × 20 cm faces was chosen as the imaging target's XY plane, which was divided into 2400 grid cells with a spacing of 0.5 cm × 0.5 cm.

The experimental setup consisted of a DS-2 series acoustic emission signal tester (Beijing Soft Island Times Technology Co., Ltd.) equipped with eight sensors evenly distributed on the imaging plane. This configuration enabled effective acquisition of acoustic emission event signal parameters in the XY plane of the granite sample. The specific sensor positions are shown as blue triangles in Fig. 10b. To ensure the stability of the sensor placement, epoxy resin was used to fix the sensor bases onto the sample surface, and petroleum jelly was applied to the ceramic contact surfaces of the probes as a coupling agent to enhance acoustic signal transmission efficiency, as shown in Fig. 10a.

Before the formal experiment, the pencil-lead break method was employed for location testing and velocity calibration to verify the response consistency of the sensor array to source signals. In the formal experiment, a hard black pencil lead with a diameter of 0.5 mm was selected and placed at a 30-degree angle to the sample surface. The pencil lead was then smoothly and quickly broken at the grid intersection points on the surface to generate acoustic emission signals. After eliminating abnormal data, a total of 485 valid acoustic emission events

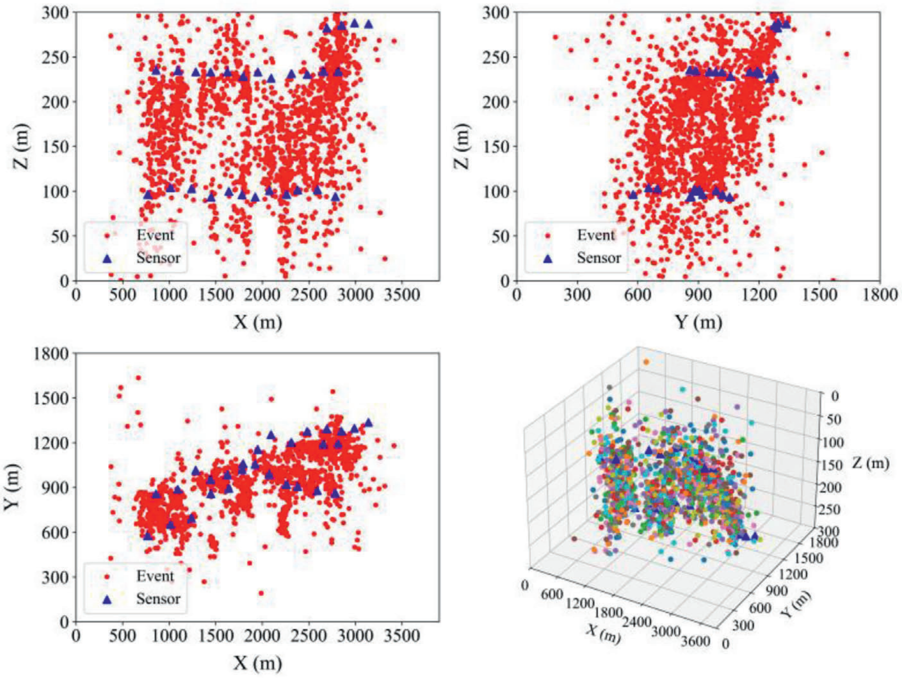

Fig. 5. Source and sensor locations for the checkboard test at XZ, YZ, ZY, and 3D views. The blue triangles and colored circles represent the sensor and source locations, respectively.

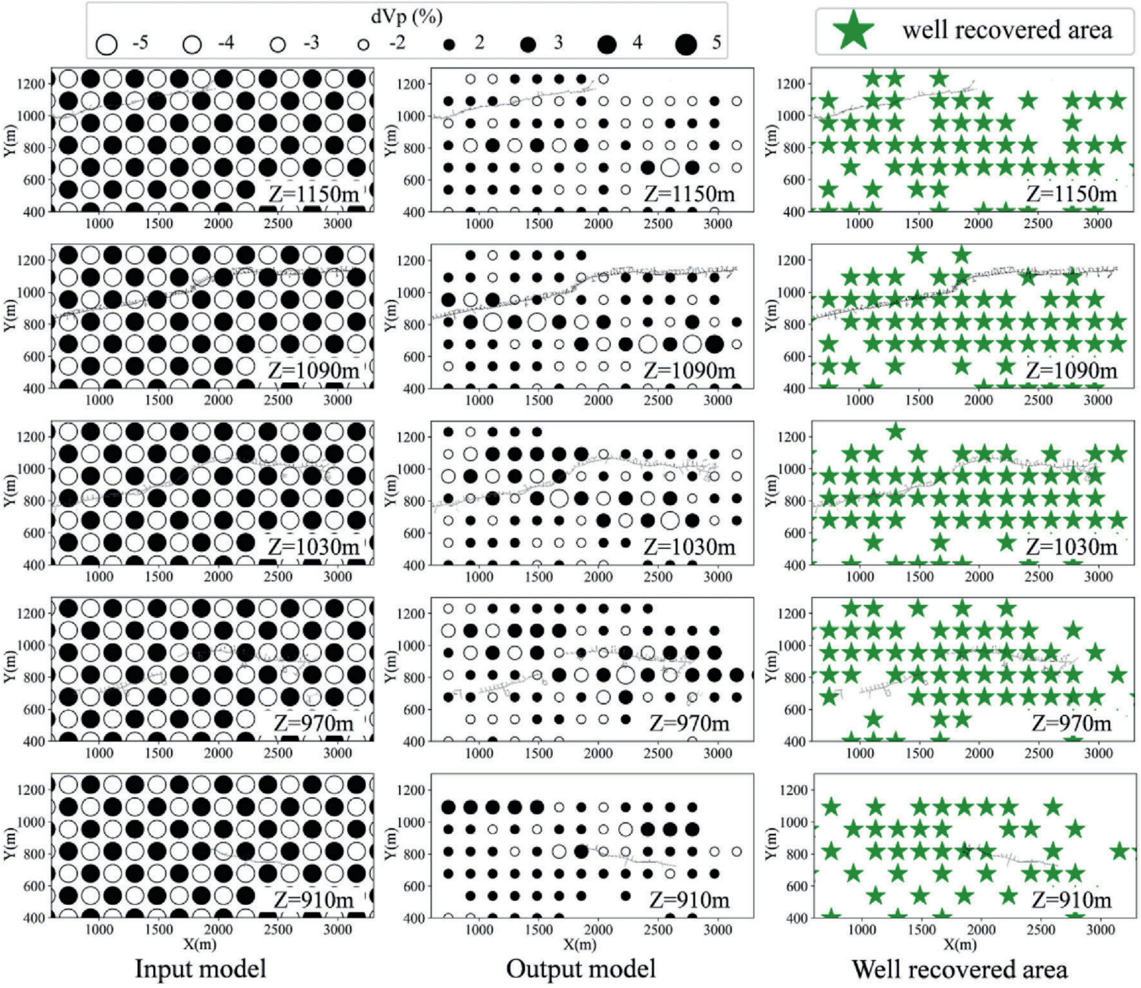

Fig. 6. Results of the checkerboard test. The left and middle columns show the input and output models, respectively, and the right column shows the well recovered areas. The black curve shows the mining tunnel.

were obtained, as shown in Fig. 10b. During signal acquisition, the gain of each channel was set to 40 dB, the trigger threshold to 100 mV, and the sampling rate to 3 MHz.

For signal processing, the AIC (Akaike Information Criterion) algorithm was first applied to automatically pick the first arrivals of the acquired P-wave signals, thereby determining the P-wave arrival times with high efficiency and accuracy. Subsequently, manual inspection was conducted to detect and correct anomalies in the automatically picked data, ensuring the high accuracy of the travel-time data.

To verify the effectiveness of the proposed method in experimental tests, both the FMM and straight-ray method were used to invert the velocity structure of the granite specimen with a hole. For the FMM method, the inputs included the coordinates of 397 valid lead-break event nodes, the observed first-arrival P-wave times, and the spatial coordinates of the sensors as multi-channel datasets. The background P-wave velocity for the 2400 grid cells of the granite specimen was set to 5000 m/s as the initial velocity model. Subsequently, the FMM algorithm was employed to iteratively solve the discrete Eikonal equation and generate a two-dimensional travel-time field of the specimen plane. Based on the Eikonal solution, ray paths were further traced backward, thereby obtaining complete ray-path and travel-time computations from each lead-break event node to all sensor nodes. Fig. 11 shows examples of typical ray paths and trave-ltime fields obtained by the FMM approach for selected events.

Furthermore, the ART algorithm was applied to iteratively update the parameters of the initial velocity model until a predefined convergence criterion was reached, while outlier parameters were removed during the process. The final two-dimensional velocity structure imaging results of the granite specimen obtained by both the FMM and straight-ray methods are shown in Fig. 12. As seen from the imaging results, the velocity distribution generated by the straight-ray method appears rather scattered, and the background velocity around the target circular hole area is somewhat chaotic, failing to accurately reconstruct the velocity structure features. In contrast, the FMM method yields a more orderly velocity distribution, with clearly defined boundaries at the circular region and a more complete, consistent background velocity, thereby enabling a more accurate reconstruction of the internal velocity structure of the granite specimen with a hole.

Additionally, most of the background P-wave velocities are around 6100 m/s, closely matching the actual granite velocity of 6110 m/s measured in this study using a non-metallic ultrasonic detector. At the same time, the abnormally low-velocity zone shown in the figure accurately reflects the real structure of the granite sample containing the hole. This demonstrates that when processing real acoustic emission lead-break experimental data for velocity structure inversion, the FMM method can provide more accurate two-dimensional velocity images compared to the straight-ray method. Moreover, the proposed imaging method can effectively invert velocity structures under real rock-sample conditions, providing a solid foundation and considerable potential for future field-scale microseismic tomography applications in mining engineering.

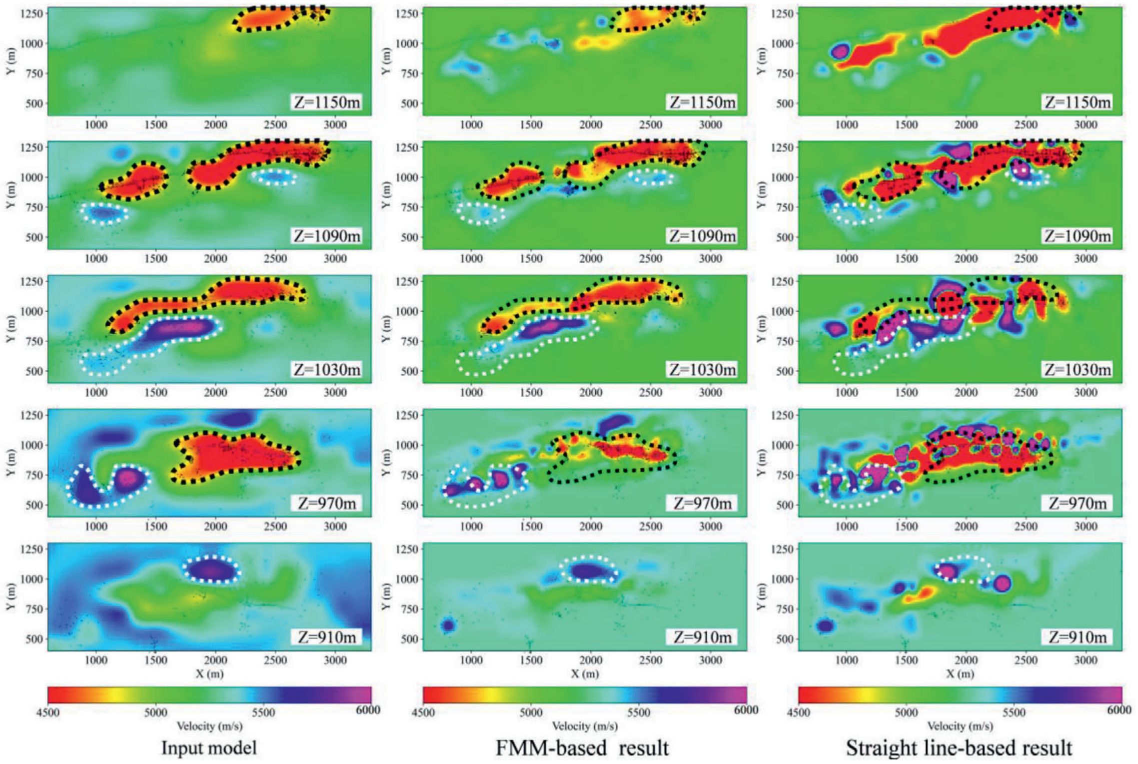

Input model

FMM-based result

Straight line-based result

Fig. 7. Results of recovery tests based on FMM and straight line. The left, middle, and right panels display the input model, FMM-based inversion result, and straight line-based inversion result, respectively. The white dashed boxes outline the high-velocity zones in the models, while the black dashed boxes indicate the low-velocity zones. The black dots and black lines represent the locations of microseismic events and the stratified tunnels, respectively.

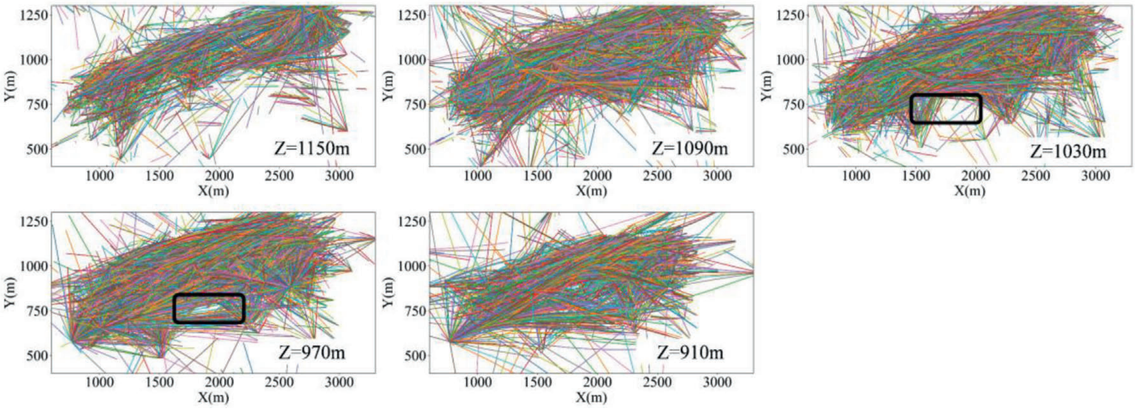

Fig. 8. Distribution of seismic rays used in this study. The colored line represents the ray that passes through the layer, and the areas within the solid black boxes have a limited ray distributions.

4. Field application

4.1. Engineering background

The Yongshaba Mine, located in Guizhou Province, China, was selected as the study area. The geographical coordinates of the mine are E106°47′32.5″–106°51′33″ and N27°08′24″–27°10′50″. With the depletion of shallow resources, ground pressure in the mine has become increasingly severe. Frequent mining disturbances disrupt the stress field, leading to stress concentration and considerable energy accumulation in the surrounding rock layers. This may result in disasters such as rock bursts, large-scale rock-mass instability, and collapses of mined-out areas. Therefore, monitoring and assessing the internal structural evolution of the mining area are of great importance for both environmental protection and engineering safety.

4.2. Engineering application

A microseismic monitoring system was established to record microseismic activity within the Yongshaba mining area. The schematic layout of the monitoring system is shown in Fig. 13. The monitoring array consists of 28 sensors arranged at the 930 m level, 1070 m level, and 1120 m level. These sensors are installed in deep boreholes with diameters of 76–80 mm and depths ranging from 9 m to 15 m. The sensors, data acquisition instruments, and master stations are interconnected using cables and fiber optics, enabling signal transmission. The dataset used in this study consists of P-wave arrival times from both blasting and microseismic events induced by mining activities between

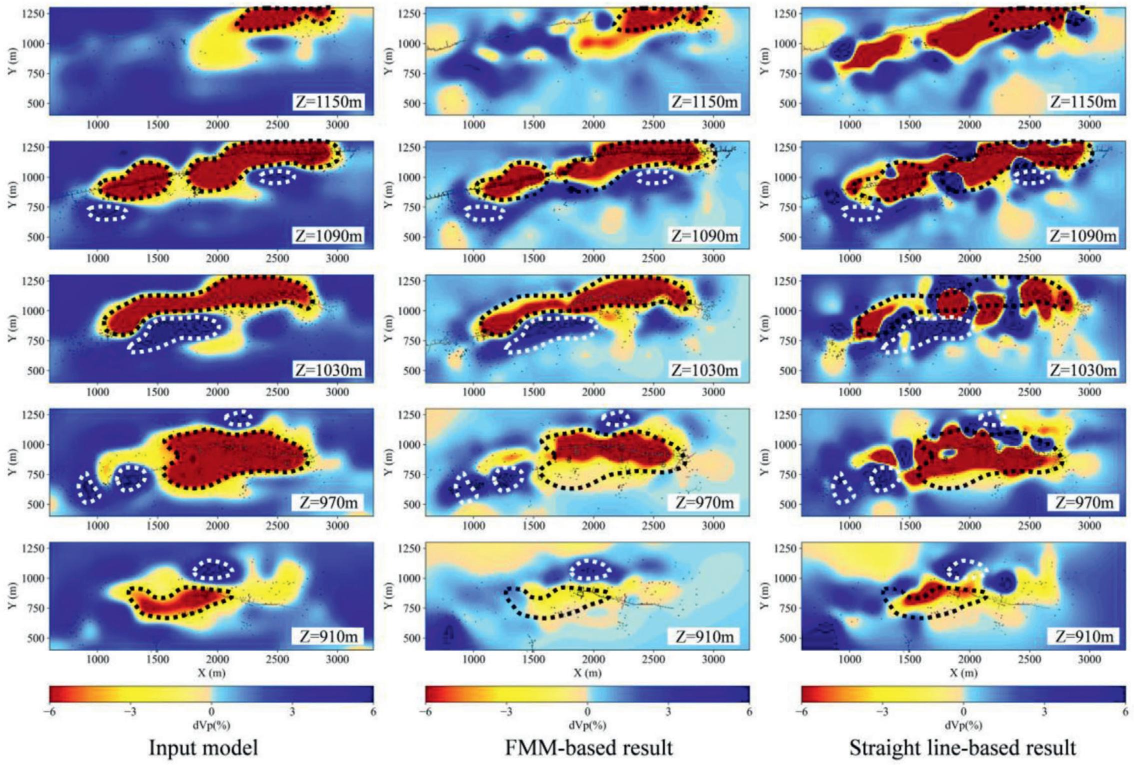

Input model

FMM-based result

Straight line-based result

Fig. 9. Velocity perturbation maps of recovery tests. The left, middle, and right panels display the input model, FMM-based inversion result, and straight line-based inversion result, respectively. The white dashed boxes outline the high-velocity perturbation zones in the models, while the black dashed boxes indicate the low-velocity perturbation zones. The black dots and black lines represent the locations of microseismic events and the stratified tunnels, respectively.

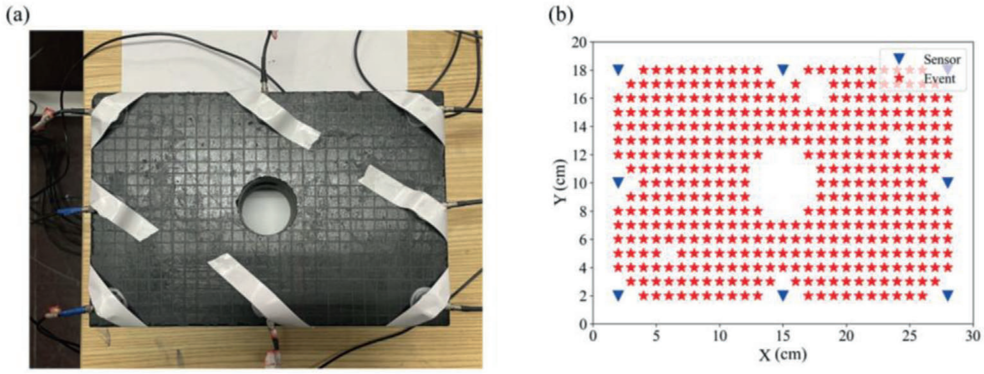

Fig. 10. Schematic of the AE pencil-lead break experiment for a granite rock sample with a hole. (a) Arrangement of the rock sample and sensors; (b) Pencil-lead break position, circular defect in the rock sample, and sensor coordinates.

January and March 2014, with approximately one-third of the events being blasts. At an engineering scale, the energy of microseismic and blasting signals rapidly attenuates with the increase of travel distance, especially the high-frequency components, which exhibit a high-speed attenuation rate. To ensure data quality, P-wave arrival times were manually picked in this study.

All events analyzed in this study were recorded by at least nine sensors, ensuring reliable data quality. Theoretically, a strong correlation exists between the distance from the source to the sensor and observed travel time. Accordingly, in the velocity structure inversion of the mining area, only the blue data points (Fig. 14) were used, while the red data points, which deviate significantly from the average velocity, were discarded. After filtering, the final dataset comprised 20,330 P-wave arrival times from 1845 well-located events, with useable arrivals accounting for more than 95% of the entire dataset. The selected microseismic events were evenly distributed across the study area, ensuring good ray coverage. Specifically, in the horizontal direction, the seismic events are distributed with a slight inclination, while in the vertical direction, they are mainly concentrated at elevations between 900 m and 1200 m. Although a few events fell outside this range, they were located farther from the study area and were therefore excluded. Based on the distribution of microseismic events, sensor locations, and ray coverage, the modeling ranges were ultimately determined to be 600–3300 m in the *X* direction, 400–1300 m in the *Y* direction, and 850–1150 m in the *Z* direction, with the internal node spacing in both the horizontal and vertical directions set to 50 m.

Determining the initial velocity model is crucial for tomographic inversion, because a well-defined initial model not only ensures accurate ray tracing but also allows the inversion process to begin closer to the “true solution”, thereby improving the likelihood of obtaining an

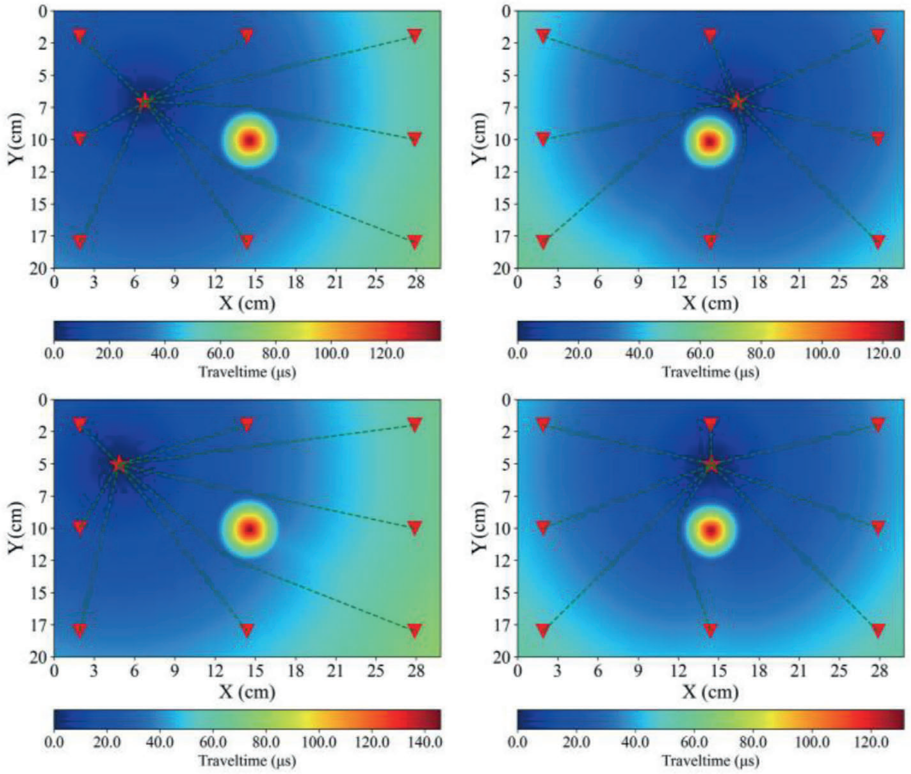

Fig. 11. Examples of typical ray paths and travel-time fields for selected pencil-lead break events. Red pentagrams mark the locations of pencil-lead break events, red triangles indicate sensor positions, green dashed lines show ray paths.

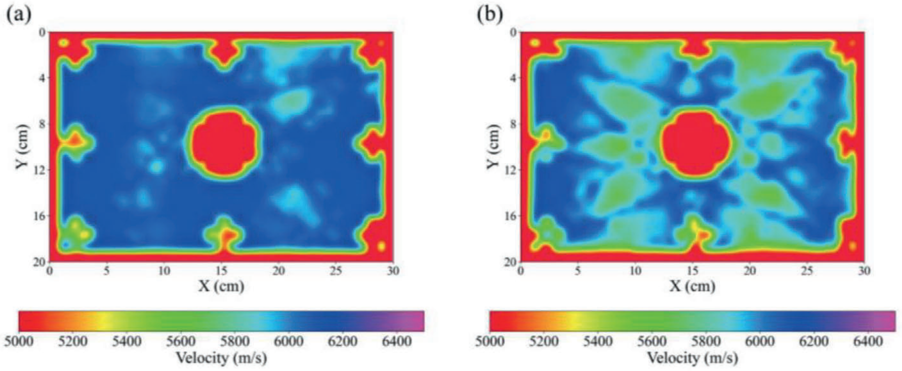

Fig. 12. Results of the 2D velocity model of the granite sample obtained by the two methods. The P-wave velocity scale is shown at the bottom. (a) FMM-based result; (b) Straight line-based result.

optimal result. According to Simmons' experimental results, within the pressure range of 0–40 MPa, the P-wave velocity increases by 200 m/s for every 10 MPa pressure increase (Simmons, 1964). For the overburden rock, the pressure increases by about 2.8 MPa for every 100 m of depth; therefore, the P-wave velocity was set to increase by 56 m/s per 100 m. According to geological data from the study area, the rock quality of the hanging wall is superior to that of the footwall in terms of strength and integrity; therefore, an additional 200 m/s was assigned to the lower part. In addition, calibration blasts conducted in the study area measured an average velocity of approximately 5200 m/s. Based on these results and simplifications, the initial velocity model was established, as shown in Fig. 15. In this model, the top layer was assigned a velocity of 5100 m/s with a gradient of 33.6 m/s per layer, while the lower three layers began at 5300 m/s with an additional 200 m/s added to each layer.

4.3. FMM tomographic imaging interpretation

The 3D velocity model of the Yongshaba mine was constructed as follows: first, the P-wave first-arrival times were filtered, retaining only high-quality data recorded by at least nine sensors and meeting physical constraints for inversion. Next, an initial velocity model was established based on the pressure–velocity relationship and the geological data. Finally, the ART was applied to the filtered travel times to obtain the final three-dimensional velocity structure of the mining area. Fig. 16 presents the imaging results for different layers, where the black dashed box on the left indicates the low-velocity zone, and the white dashed box represents the high-velocity zone. The main features of the inverted model fall largely within the well-recovered areas outlined earlier, thereby indicating the reliability of the results. The FMM tomographic imaging on the left reveals a large, continuous low-velocity zone surrounded by several small, dispersed high-velocity areas, which are

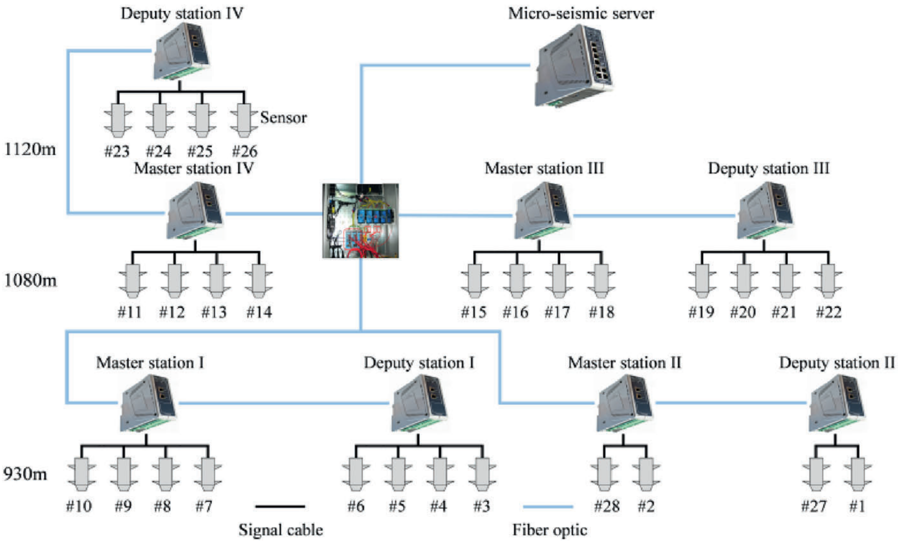

Fig. 13. Schematic diagram of the microseismic monitoring system.

clearly distributed along the mining tunnels. Overall, the distribution of low-velocity and high-velocity zones aligns with the discontinuous trends and shapes observed in the model. The formation of low-velocity zones can be caused by stress release and rock fracturing due to the structural planes and surrounding mining activities. Then, the extensive goaves created by ore extraction obstruct seismic wave propagation, resulting in relatively low velocity values within and around these goaves. Additionally, the microseismic events induced by mining activities are primarily distributed within or near the low-velocity zones, indicating a close correlation between the low-velocity anomalies and goaves. The high-velocity zones are likely associated with local stress concentrations caused by regional stress redistribution. In this process, the surrounding rock mass bears the load that would otherwise have been supported by the low-velocity zones, thereby driving the redistribution of regional stress. Since local stress concentration is a major cause of engineering disasters such as rock bursts, high-velocity zones in practical applications can therefore be regarded as potentially hazardous areas.

The mining plan provides an effective means of corroborating the above assumptions. The specific mining plan of the Yongshaba mine is shown in Fig. 17. It can be seen that the northern part of the ore body, at elevations between 1120 and 1170 m, has already been mined or is currently being mined, while the southern part remains to be excavated. Consequently, the surrounding rock in the southern part of this elevation range remains relatively intact, whereas that in the north around the 1150 m level is significantly fractured, as evidenced by the low-velocity zone in the 1150 m layer shown in Fig. 16. These fractured rocks have generated a low-velocity anomaly in the northern horizontal section, consistent with the tomographic imaging results. The mining plan further indicates that large-scale extraction is underway in the ore body at elevations between 920 and 1120 m. Such mining activities may lead to stress release, rock fracturing, and the formation of goaves, thereby producing significant low-velocity zones. The corresponding tomographic imaging indeed confirms the presence of these prominent low-velocity zones.

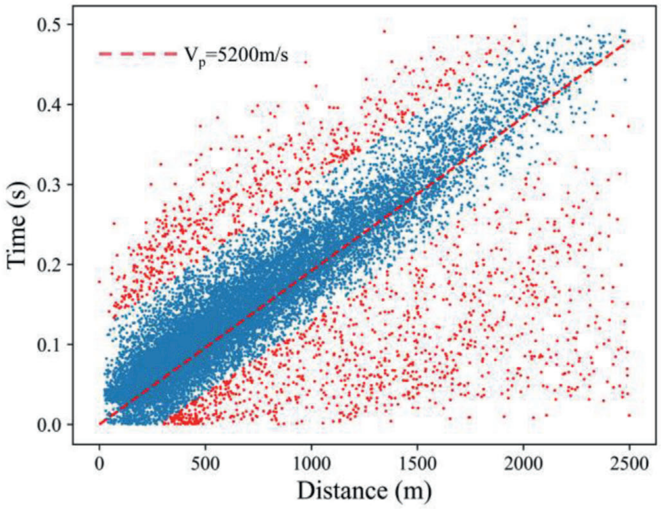

Fig. 14. Correlation between straight line distance and travel time of the original dataset. The red and blue points represent discarded data and selected data, respectively. The red solid line indicates the P-wave velocity (*Vp*) used for the initial location of the seismic events.

4.4. *Velocity structure evolution during the mining process*

In large-scale underground engineering projects, frequent human activities can significantly change the subsurface structure. Time-lapse velocity models offer an effective means of studying the evolution of

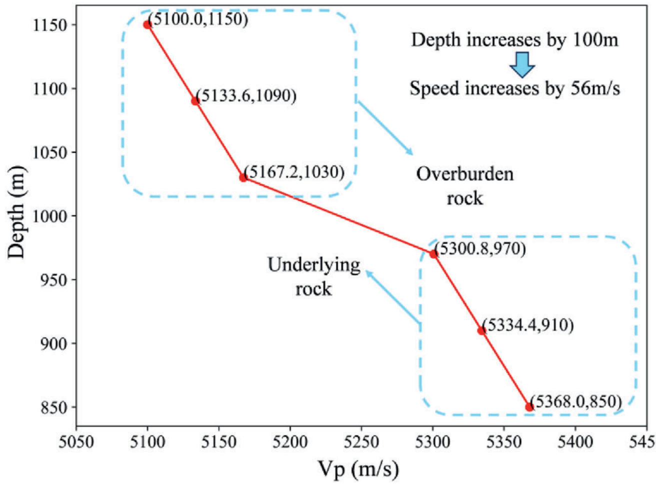

Fig. 15. Initial velocity model for velocity imaging. The numbers in the brackets indicate *Vp* values and their corresponding depths.

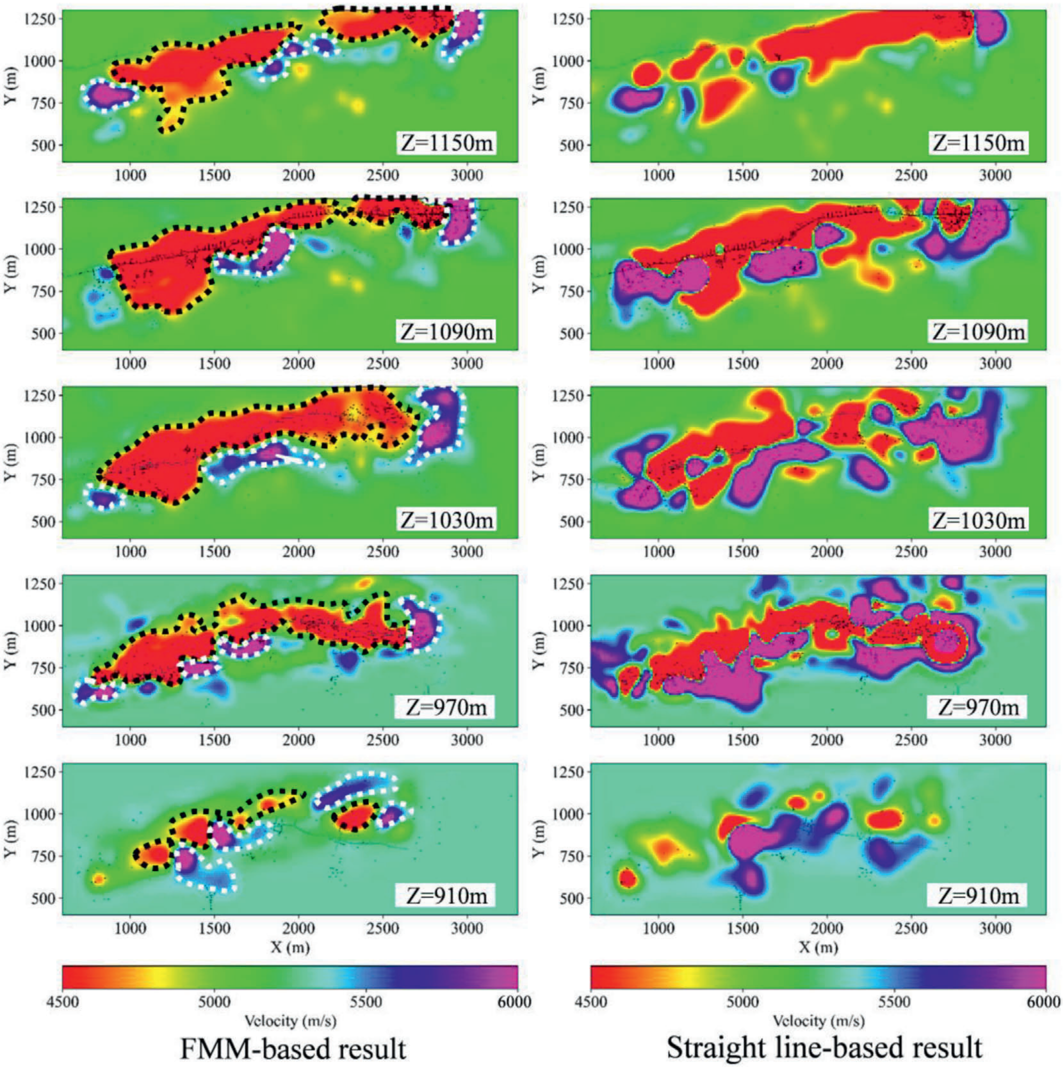

Fig. 16. Tomographic imaging result of the Yongshaba mine based on the FMM and straight line ray tracing. The white dashed boxes outline the high-velocity zones in the models, while the black dashed boxes indicate the low-velocity zones. The black dots and black lines represent the locations of microseismic events and the stratified tunnels, respectively.

the underground structure. For this purpose, the microseismic data collected between January and April 2014 were divided into three sub-intervals: January–February, February–March, and March–April. The three sub-datasets contain 8120, 12,258, and 12,210 P-wave ray paths, respectively. Fig. 18 presents the absolute velocities obtained from these three datasets, while Fig. 19 shows their corresponding velocity perturbations. Although significant differences exist in the seismic data across the three datasets, the fundamental features of the images obtained from their respective inversions are highly similar. For example, the datasets from January–February and March–April contain no overlapping seismic events, yet the velocity perturbations and velocity images derived from them exhibit a high degree of similarity. The results

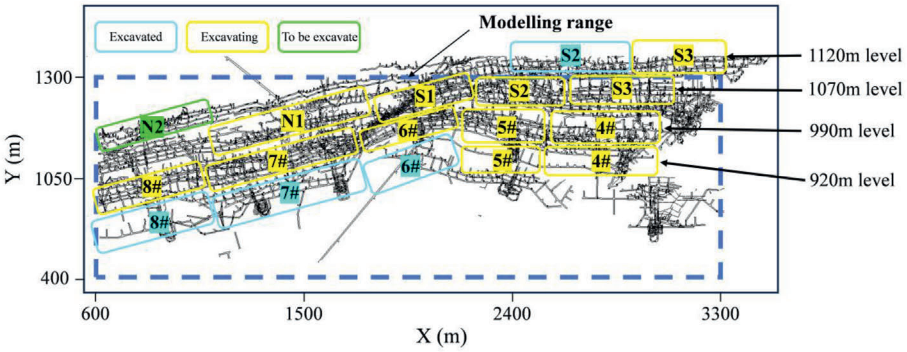

Fig. 17. Mining plan for the Yongshaba mine. The black curves show the mining tunnels. The number within the colored boxes correspond to the panel numbers.

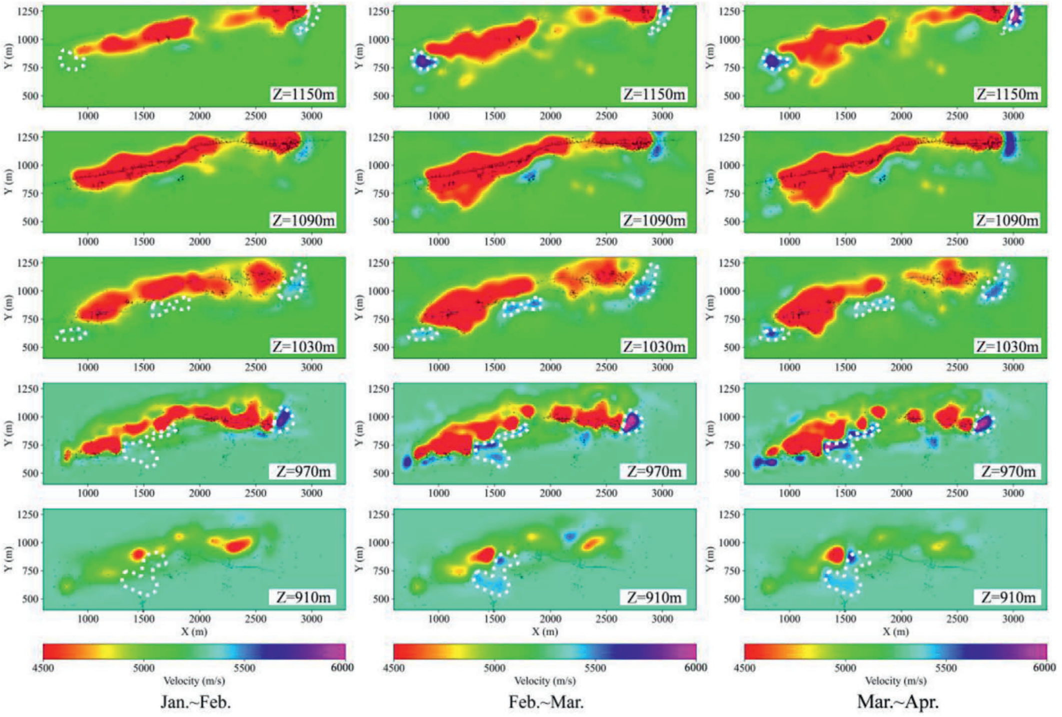

Fig. 18. Absolute velocity map based on different time intervals. The white dashed box indicates the varying high-velocity zone. The black dots and black lines represent the locations of microseismic events and the stratified tunnels, respectively.

from the three datasets exhibit only minor differences in detail, strongly demonstrating that the proposed method can accurately characterize the subsurface structure while confirming the stability and reliability of the results.

For the low-velocity zones at the $Z = 1150$ m and $Z = 1090$ m levels, the velocity perturbations exhibit only minor variations overall, indicating that the rock mass at these depths has experienced limited disturbance. This observation is consistent with the mining plan shown

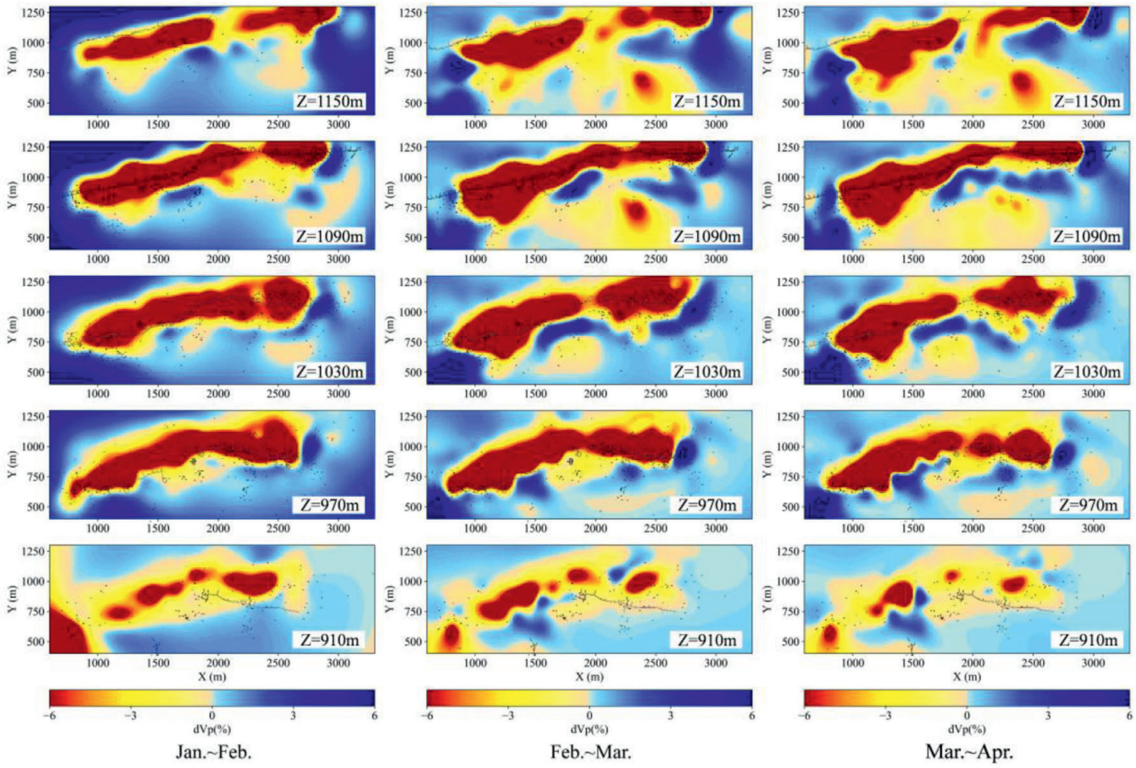

Fig. 19. Velocity perturbation map based on different time intervals. The black dots and black lines represent the locations of microseismic events and the stratified tunnels, respectively.

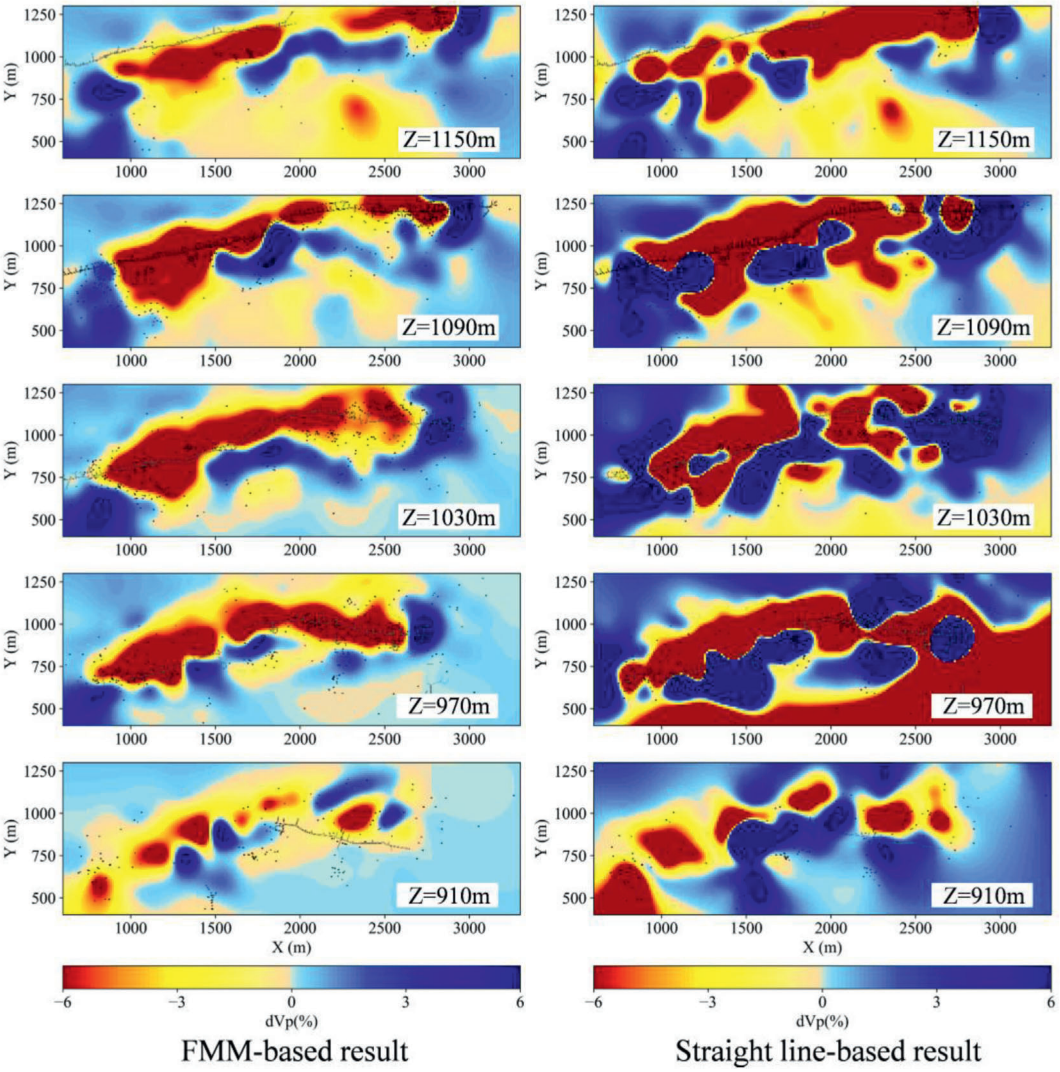

Fig. 20. Velocity perturbation map of the Yongshaba mine based on the FMM and straight line ray tracing techniques. The black dots and black lines represent the locations of microseismic events and the stratified tunnels, respectively.

in Fig. 17. Significant microseismic activity is observed in the low-velocity zones at these two levels, largely induced by mining operations at the 1020 m level. At the $Z = 970$ m and $Z = 1030$ m levels, both the extent and magnitude of the low-velocity zones show an increasing trend, which is closely related to the large-scale mining activities occurring at the 990 m level and its adjacent areas. Moreover, the magnitude and extent of these low-velocity zones fluctuate significantly over time, suggesting that as they expand outward, processes such as rock fracturing and cracking occur, thereby triggering intense seismic activity.

Local high-velocity zones exhibit significant variations over different periods, as highlighted by the white dashed boxes in Fig. 18. At the $Z = 1150$ m level, the high-velocity zones at $X = 800$ m and $X = 3000$ m expand gradually over time; at the $Z = 1090$ m and $Z = 1030$ m levels, the high-velocity zone at $X = 3{,}000$ m continues to grow. In contrast, at $X = 1800$ m a high-velocity zone first appears and then shrinks, while at $X = 700$ m a new one emerges. At the $Z = 970$ m level, the high-velocity zone at $X = 2800$ m continues to expand while another gradually develops at $X = 1500$ m; moreover, at the $Z = 910$ m level, a significant high-velocity zone emerges near $X = 1600$ m. These dramatic spatio-temporal changes in the high-velocity zones reflect the frequent stress redistributions induced by mining activities.

5. Discussion

5.1. Imaging result comparison among different ray tracing techniques

Straight-line ray tracing has long been the most widely used approach in mining engineering and rock mechanics. For instance, Jiang et al. (2014) applied straight-line tomography to concrete at an experimental scale for damage localization but achieved relatively low resolution. Cai et al. (2014) used straight-line connections combined with the simultaneous iterative reconstruction technique (SIRT) for passive and active source tomography in the Yima coal mine, successfully analyzing underground stress distribution. Li et al. (2017) further emphasized the need for tomography methods suitable for complex geological conditions in order to meet safety monitoring requirements. Although widely applied, straight-line ray tracing suffers from inherent limitations under heterogeneous conditions. In contrast, FMM offers superior accuracy, efficiency, and adaptability, as its wavefront-expansion principle is consistent with seismic wave propagation laws.

To evaluate the advantages of the FMM, comparative studies were conducted through synthetic tests and field applications. In the recovery test (Figs. 7 and 9), the FMM successfully reconstructed the prominent low-velocity zones and surrounding high-velocity anomalies, whereas

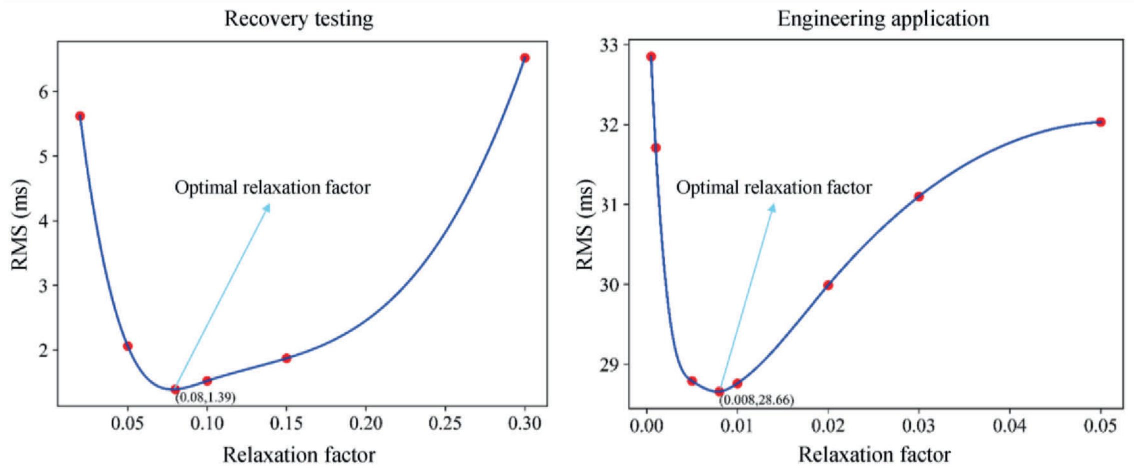

Fig. 21. Relaxation factor trade-off curves for the recovery test and engineering application. Solid red dots represent the fitting points, while the numbers beside the optimal relaxation factor denote its value and the corresponding RMS.

straight-line tomography showed large discrepancies, indicating lower reliability. Engineering application results (Figs. 16 and 20) show that the straight-line method produces scattered low-velocity distributions with anomalous high-velocity patches embedded within, which are inconsistent with the actual effects of mining activities. In contrast, the FMM results reveal continuous low-velocity zones distributed along mining tunnels, highly consistent with the excavation plan. The straight-ray method, constrained by the assumption of linear propagation, fails to account for ray bending in heterogeneous media. As a result, its reconstructions are prone to elongation, streaking artifacts, and misplaced or fragmented anomalies, particularly in regions with sparse or unidirectional ray coverage (e.g., $Z = 1030$ m and $Z = 970$ m). By contrast, the FMM-based method incorporates wavefront expansion and naturally follows bent raypaths, yielding forward modeling that better represents the true physics of seismic wave travel. Consequently, FMM consistently produces sharper anomaly boundaries, fewer artifacts, and more geologically reasonable distributions. Even in poorly covered areas, where both methods face limitations, the FMM still preserves the main structures, whereas the straight-ray results deteriorate severely. Quantitatively, the travel-time residual RMS of 28.66 ms for FMM compared to 35.22 ms for the straight-ray method further confirms its superiority. These results demonstrate that while ray coverage sets the overall resolution limit, FMM-based inversion achieves solutions much closer to this limit, offering significant improvements in accuracy and reliability over straight-ray tomography.

More importantly, such high-precision velocity imaging can directly serve engineering needs: it enables the early identification of goaves (mined-out zones), optimizes tunnel layout and excavation strategies,

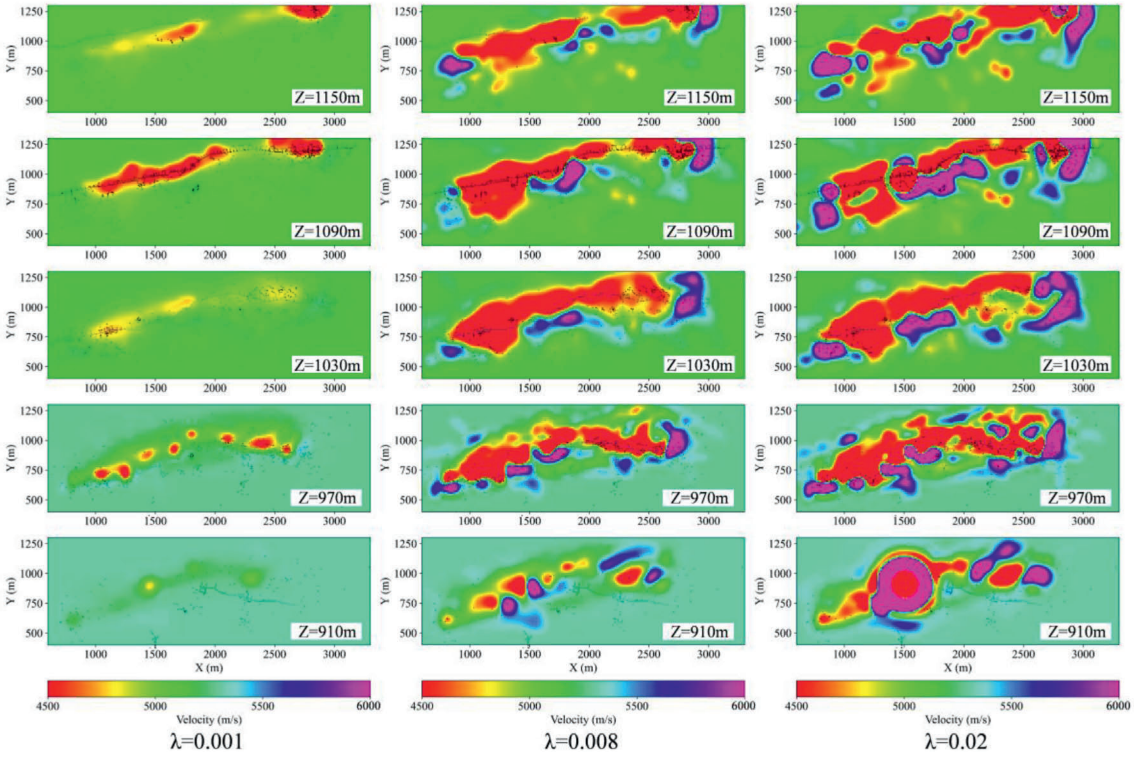

Fig. 22. Comparison of imaging results based on different relaxation factors. The black dots and black lines represent the locations of microseismic events and the stratified tunnels, respectively.

and assists in risk prediction for high-stress or unstable areas. In addition, the FMM-ART framework shows great potential for integration with real-time monitoring systems. By interfacing with continuous data streams such as microseismic monitoring, in-situ stress sensors, and surface subsidence observations, this method can dynamically update velocity models during imaging and capture evolving changes in subsurface structures. At the same time, as a physics-based imaging approach, it provides a solid physical foundation and high-quality input data for AI-based recognition and hazard prediction systems. AI algorithms can utilize the 3D velocity fields and stress evolution patterns derived from FMM-ART for pattern recognition and risk forecasting, thereby overcoming the limitations of approaches that rely solely on empirical data. With the increasing emphasis on intelligent mining and safety management, this integration model will greatly enhance the practicality and reliability of dynamic hazard prediction and long-term mine safety management.

5.2. *Effect of the ART relaxation factor*

The relaxation factor in ART plays a critical role in balancing convergence stability and reconstruction accuracy. Previous studies (Herman and Meyer, 1993; Mueller et al., 1997; Mesquita et al., 2010) indicate that selecting appropriate values within the range of 0–2 ensures stable convergence, particularly when handling noisy data. In this study, trade-off curves between the travel-time residual RMS and relaxation factor were established for both synthetic recovery tests and field applications (Fig. 21). The optimal values were determined to be 0.08 and 0.008, yielding minimal RMS values of 1.39 ms and 28.66 ms, respectively.

Comparative reconstructions with different λ values (Fig. 22) further demonstrate the impact of the relaxation factor. When $\lambda = 0.008$, the low-velocity zones align well with the mining tunnels, with high-velocity zones reasonably distributed around them. In contrast, at $\lambda = 0.001$, the reconstructed low-velocity zones deviate significantly from the mining plan and no high-velocity zones appear, while at $\lambda = 0.02$, numerous anomalous high-velocity patches are generated.

Nevertheless, using a fixed relaxation factor in iterative processes has inherent limitations. A dynamic selection strategy could further improve reconstruction quality. Moreover, current implementations distribute travel-time residuals uniformly across all cells, although in practice, defective cells may exert disproportionate influence. Future work should explore adaptive weighting schemes that account for heterogeneous contributions of different cells to enhance inversion accuracy.

6. Conclusion

This study addresses the limitations of conventional straight-ray tomography, which violates the eikonal equation in heterogeneous media. we proposed a 3D velocity imaging method for mines that integrates the Fast Marching Method (FMM) for accurate ray tracing with the Algebraic Reconstruction Technique (ART) for velocity inversion. The method was rigorously validated through synthetic experiments and applied to field data from the Yongshaba mine, with the following main conclusions:

(1) The proposed method introduces FMM-based bent-ray tracing into mine-scale tomography for the first time, ensuring accurate and efficient travel-time calculation in complex media. Coupled with ART, the method enables the reconstruction of high-accuracy 3D velocity models.

(2) Synthetic checkerboard tests, recovery tests, laboratory Lead-Break experiments, and field applications confirm the method's superiority over straight-line tomography. The travel-time residual RMS values of 1.39 ms (recovery test) and 28.66 ms (field application) represent reductions of 76.6% and 18.6%, respectively, compared with the straight-line approach.

(3) The 3D P-wave velocity image of the Yongshaba mine reveals pronounced velocity discontinuities: low-velocity zones correspond to goaves, stress release, and mining-induced fracturing, whereas high-velocity zones reflect local stress concentrations. The strong alignment of these velocity anomalies with mining activities indicates that the proposed method provides reliable information for assessing rock mass stability and guiding mine planning and safety management. Furthermore, the proposed FMM-ART framework shows strong potential for extension, including integration with real-time monitoring systems, which would enhance its applicability to dynamic hazard prediction and long-term mine safety management.

CRediT authorship contribution statement

Jie Yang: Writing – review & editing, Writing – original draft, Software, Methodology, Formal analysis, Data curation. **Xueyi Shang:** Writing – review & editing, Supervision, Project administration, Methodology, Conceptualization. **Linghao Liu:** Writing – review & editing, Methodology, Formal analysis. **Yi Wang:** Writing – review & editing, Supervision, Methodology, Conceptualization. **Xibing Li:** Supervision, Project administration, Data curation, Conceptualization.

Declaration of competing interest

The authors declare that they have no known competing financial interests or personal relationships that could have appeared to influence the work reported in this paper.

Acknowledgements

All authors would like to acknowledge the financial support provided by the National Natural Science Foundation of China (Nos. 52574137, 52004041 and U21A2030).

References

Aki, K., Christoffersson, A., Husebye, E.S., 1977. Determination of the three-dimensional seismic structure of the lithosphere. J. Geophys. Res. 82, 277–296. https://doi.org/10.1029/JB082i002p00277.

Bhagade, N.V., Murthy, V.M.S.R., Budi, G., 2021. Measurement and control of seismic effects in large scale dragline bench blasts-An approach. Measurement 168, 108390. https://doi.org/10.1016/j.measurement.2020.108390.

Brantut, N., 2018. Time-resolved tomography using acoustic emissions in the laboratory, and application to sandstone compaction. Geophys. J. Int. 213 (3), 2177–2192. https://doi.org/10.1093/gji/ggy068.

Cai, W., Dou, L., Cao, A., Gong, S., Li, Z., 2014. Application of seismic velocity tomography in underground coal mines: a case study of Yima mining area, Henan, China. J. Appl. Geophys. 109, 140–149. https://doi.org/10.1016/j.jappgeo.2014.07.021.

Chen, C., Zhao, D., Wu, S., 2015. Tomographic imaging of the Cascadia subduction zone: constraints on the Juan de Fuca slab. Tectonophysics 647, 73–88. https://doi.org/10.1016/j.tecto.2015.02.012.

Chen, Y., Chen, Y., Fomel, S., Savvaidis, A., Saad, O.M., Oboué, Y.A.S.I., 2023. Pyekfmm: a python package for 3D fast-marching-based traveltime calculation and its applications in seismology. Seismol Res. Lett. 94 (4), 2050–2059. https://doi.org/10.1785/0220230042.

Dong, L., Tong, X., Ma, J., 2021. Quantitative investigation of tomographic effects in abnormal regions of complex structures. Eng. Plast. 7 (7), 1011–1022. https://doi.org/10.1016/j.eng.2020.06.021.

Dong, L., Liu, C., Yang, L., Fan, F., Yuan, W., Hao, C., 2024. Acoustic parameters and wave velocity field evolution characteristics in the high-stress region of granite. Measurement 237, 115271. https://doi.org/10.1016/j.measurement.2024.115271.

Dziewonski, A.M., Hager, B.H., O'Connell, R.J., 1977. Large-scale heterogeneities in the lower mantle. J. Geophys. Res. 82, 239–255. https://doi.org/10.1029/JB082i002p00239.

Herman, G.T., Meyer, L.B., 1993. Algebraic reconstruction techniques can be made computationally efficient (positron emission tomography application). Ieee T. Med. Imaging. 12 (3), 600–609. https://doi.org/10.1109/42.241889. No.3.

Huang, J., Zhao, D., 2006. High-resolution mantle tomography of China and surrounding regions. J. Geophys. Res. Solid Earth 111 (B9), B09305. https://doi.org/10.1029/2005jb004066.

Hwang, Y.K., Ritsema, J., Keken, P.E., Saskia, G., Elinor, S., 2011. Wavefront healing renders deep plumes seismically invisible. Geophys. J. Int. 187 (1), 273–277. https://doi.org/10.1111/j.1365-246X.2011.05173.x.

Jiang, Y., Xu, F., Xu, B., Suárez, E., Gallego, A., 2014. Application of acoustic emission tomography technology in concrete structures. J. Southeast Univ. Nat. Sci. Ed. 44 (4), 822–825 (in Chinese).

Julian, B.R., Gubbins, D., 1977. Three-dimensional seismic ray tracing. J. Geophys. 43 (1), 95–113.

Li, N., Wang, E., Ge, M.C., 2017. Microseismic monitoring technology and its application status and prospects at coal mines. J. China Coal Soc. 42 (S1), 83–96 (in Chinese).

Liu, L., Li, S., Zheng, M., Wang, D., Chen, M., Zhou, J., Yan, T., Shi, Z., 2024. Inverting the rock mass P-wave velocity field ahead of deep buried tunnel face while borehole drilling. Int. J. Min. Sci. Technol. 34 (5), 681–697. https://doi.org/10.1016/j.ijmst.2024.06.001.

Łukasz, W., Joanna, K., Małgorzata, K., 2021. The influence of mining factors on seismic activity during longwall mining of a coal seam. Int. J. Min. Sci. Technol. 31 (3), 429–437. https://doi.org/10.3969/j.issn.2095-2686.2021.03.009.

Mesquita, J., Matela, N., Oliveira, N., Martins, M.V., Almeida, P., 2010. Choosing the ART relaxation parameter for Clear-PEM 2D image reconstruction. Comput. Methods Progr. Biomed. 98 (2), 183–190. https://doi.org/10.1016/j.cmpb.2009.11.010.

Mueller, K., Yagel, R., Cornhill, J.F., 1997. The weighted-distance scheme: a globally optimizing projection ordering method for ART. Ieee T. Med. Imaging. 16 (2), 223–230. https://doi.org/10.1109/42.563668.

Niu, Z., Qiu, Z., Zhu, H., Che, A., Huang, S., Wang, H., Han, Z., 2025. Bayesian approach for uncertainty quantification in elastic wave tomography of concrete structures. Measurement 243, 116327. https://doi.org/10.1016/j.measurement.2024.116327.

O'Connell, D.R.H., Ma, S., Archuleta, R.J., 2007. Influence of dip and velocity heterogeneity on reverse and normal-faulting rupture dynamics and near-fault ground motions. Bull. Seismol. Soc. Am. 97 (6), 1970–1989. https://doi.org/10.1103/PhysRevE.79.016110.

Rawlinson, N., Sambridge, M., 2004. Multiple reflection and transmission phases in complex layered media using a multistage fast marching method. Geophysics 69 (5), 1338–1350. https://doi.org/10.1190/1.1801950.

Sethian, J.A., 1996. A fast marching level set method for monotonically advancing fronts. P. Natl. Acad. Sci. Usa. 93 (4), 1591–1595. https://doi.org/10.1073/pnas.93.4.1591.

Seya, K., Suzuki, I., Fujiwara, H., 1979. The change in ultrasonic wave velocities in triaxially stressed brittle rock. J. Phys. Earth 27 (5), 409. https://doi.org/10.4294/jpe1952.27.409-421.

Simmons, G., 1964. Velocity of compressional waves in various minerals at pressures to 10 kilobars. J. Geophys. Res. 69 (6), 1117–1121.

Song, C., Lu, C., Chen, C., Zhan, Z., 2024. Three-dimensional velocity structure of a coal mine revealed by induced microseismic traveltime data. Int. J. Min. Sci. Technol. 173, 105633. https://doi.org/10.1016/j.ijrmms.2023.105633.

Vidale, J., 1988. Finite-difference calculation of travel times. Bull. Seismol. Soc. Am. 78 (6), 2062–2076.

Vidale, J.E., 1989. Finite-difference calculation of traveltimes in 3D. Geophysics 55 (5), 521–526. https://doi.org/10.1190/1.1442863.

Wang, Z., Li, X., Zhao, D., Shang, X., Dong, L., 2018. Time-lapse seismic tomography of an underground mining zone. Int. J. Min. Sci. Technol. 107, 136–149. https://doi.org/10.1016/j.ijrmms.2018.04.038.

Wang, F., Xie, X., Yang, L., Pei, Z., Dong, L., 2023. Nondestructive velocity structure reconstruction for complex rock mass using 3-D acoustic emission tomography. Ieee. Sens. J. 23 (2), 27490–27499. https://doi.org/10.1109/JSEN.2023.3301671.

Wang, Y., Wu, G., Kong, D., 2025. Characteristics of rock strength failure and identification of hazardous areas in the roof of deep mining stope. Eng. Fail. Anal. 167, 109027. https://doi.org/10.1016/j.engfailanal.2024.109027.

Young, R., Maxwell, S.C., 1992. Seismic characterization of a highly stressed rock mass using tomographic imaging and induced seismicity. J. Geophys. Res. Solid Earth 97 (B9), 12361–12373. https://doi.org/10.1029/92JB00678.

Zhao, D., 2001. New advances of seismic tomography and its applications to subduction zones and earthquake fault zones: a review. Isl. Arc 10 (1), 68–84. https://doi.org/10.1046/j.1440-1738.2001.00291.x.

Zhou, K., Dou, L., Li, X., Song, S., Cao, J., Bai, J., Ma, X., 2022. Coal burst and mining-induced stress evolution in a deep isolated main entry area–A case study. Eng. Fail. Anal. 137, 106289. https://doi.org/10.1016/j.engfailanal.2022.106289.

Ziegler, M., Reiter, K., Heidbach, O., Zang, A., Kwiatek, G., Stromeyer, D., Dahm, T., Dresen, G., Hofmann, G., 2015. Mining-induced stress transfer and its relation to a 19 seismic event in an ultra-deep South African gold mine. Pure. Appl. Geophys. 172, 2557–2570. https://doi.org/10.1007/s00024-015-1033-x.